The Astrophysical Journal, 955:142 (12pp), 2023 October 1 https://doi.org/10.3847/1538-4357/aced0b

FAST Observations of FRB 20220912A: Burst Properties and Polarization Characteristics

Yong-Kun Zhang[1,2], Di Li[1,2,3,4], Bing Zhang[5,6], Shuo Cao[2,7], Yi Feng[3], Wei-Yang Wang[2,8], Yuanhong Qu[5,6], Jia-Rui Niu[1,2], Wei-Wei Zhu[1], Jin-Lin Han[1], Peng Jiang[1,9], Ke-Jia Lee[1,8], Dong-Zi Li[10], Rui Luo[11,12], Chen-Hui Niu[1], Chao-Wei Tsai[1], Pei Wang[1], Fa-Yin Wang[13,14], Zi-Wei Wu[1], Heng Xu[1], Yuan-Pei Yang[15,16], Jun-Shuo Zhang[1,2], De-Jiang Zhou[1,2], and Yu-Hao Zhu[1,2]

[1] National Astronomical Observatories, Chinese Academy of Sciences, Beijing 100101, People's Republic of China; ykzhang@nao.cas.cn, dili@nao.cas.cn
[2] University of Chinese Academy of Sciences, Beijing 100049, People's Republic of China
[3] Research Center for Intelligent Computing Platforms, Zhejiang Laboratory, Hangzhou 311100, People's Republic of China
[4] NAOC-UKZN Computational Astrophysics Centre, University of KwaZulu-Natal, Durban 4000, South Africa
[5] Nevada Center for Astrophysics, University of Nevada, Las Vegas, NV 89154, USA; bing.zhang@unlv.edu
[6] Department of Physics and Astronomy, University of Nevada, Las Vegas, NV 89154, USA
[7] Yunnan Observatories, Chinese Academy of Sciences, Kunming 650216, People's Republic of China
[8] Department of Astronomy, Peking University, Beijing 100871, People's Republic of China
[9] CAS Key Laboratory of FAST, National Astronomical Observatories, Chinese Academy of Sciences, Beijing 100101, People's Republic of China
[10] Cahill Center for Astronomy and Astrophysics, MC 249-17, California Institute of Technology, Pasadena, CA 91125, USA
[11] CSIRO Space and Astronomy, PO Box 76, Epping, NSW 1710, Australia
[12] Department of Astronomy, School of Physics and Materials Science, Guangzhou University, Guangzhou 510006, People's Republic of China
[13] School of Astronomy and Space Science, Nanjing University, Nanjing 210093, People's Republic of China
[14] Key Laboratory of Modern Astronomy and Astrophysics (Nanjing University), Ministry of Education, People's Republic of China
[15] South-Western Institute for Astronomy Research, Yunnan University, Kunming, Yunnan 650504, People's Republic of China
[16] Purple Mountain Observatory, Chinese Academy of Sciences, Nanjing, Jiangsu 210023, People's Republic of China
Received 2023 April 27; revised 2023 July 26; accepted 2023 August 1; published 2023 September 27

Abstract

We report the observations of FRB 20220912A using the Five-hundred-meter Aperture Spherical radio Telescope. We conducted 17 observations totaling 8.67 hr and detected a total of 1076 bursts with an event rate up to 390 hr^{-1}. The cumulative energy distribution can be well described using a broken power-law function with the lower- and higher-energy slopes of -0.38 ± 0.02 and -2.07 ± 0.07, respectively. We also report the *L*-band (1–1.5 GHz) spectral index of the synthetic spectrum of FRB 20220912A bursts, which is -2.6 ± 0.21. The average rotation measure value of the bursts from FRB 20220912A is -0.08 ± 5.39 rad m^{-2}, close to 0 rad m^{-2} and was relatively stable over 2 months. Most bursts have nearly 100% linear polarization. About 45% of the bursts have circular polarization with Signal-to-Noise ratio > 3, and the highest circular polarization degree can reach 70%. Our observations suggest that FRB 20220912A is located in a relatively clean local environment with complex circular polarization characteristics. These various behaviors imply that the mechanism of circular polarization of FRBs likely originates from an intrinsic radiation mechanism, such as coherent curvature radiation or inverse Compton scattering inside the magnetosphere of the FRB engine source (e.g., a magnetar).

Unified Astronomy Thesaurus concepts: Radio transient sources (2008)

Supporting material: machine-readable table

1. Introduction

Fast radio bursts (FRBs) are a type of astronomical phenomenon characterized by brief, intense pulses of radio waves from unknown sources. Since their discovery in 2007 (Lorimer et al. 2007), FRBs have remained a mystery, and their origins are still unknown.

To gain further understanding of the origins and radiation mechanisms involved, it is crucial to conduct statistical analysis and investigate the properties of a large sample of bursts. FRBs are empirically classified into two categories: non-repeating FRBs and repeating FRBs, with the latter accounting for a small fraction of the entire FRB population, and only a handful of them exhibiting event rates of several tens to hundreds per hour, such as FRB 20121102A (Li et al. 2021; Jahns et al. 2023), FRB 20200120E (Nimmo et al. 2023), and FRB 20201124A (Xu et al. 2022; Zhang et al. 2022b). The study of FRB polarization may reveal the complexity of the local environment. FRB 20121102A and FRB 20190520B both show exceptionally high and variable rotation measure (RM; Michilli et al. 2018; Hilmarsson et al. 2021a; Anna-Thomas et al. 2023), while FRB 20201124A displays short-time irregular RM oscillations (Xu et al. 2022). The RM variation of FRB 20180916B also exceeded 40% (Mckinven et al. 2023a). Recently, CHIME reported measurements of the polarization of 12 repeating FRBs, finding that a significant proportion of FRBs experience RM changes of tens to hundreds within months (Mckinven et al. 2023b). These facts suggest that most FRB progenitors may be located in a complex, dynamically evolving magnetized environment, such as a supernova remnant, a pulsar wind nebula, or a binary system with a massive companion star (Feng et al. 2022a; Wang et al. 2022a; Yang et al. 2023; Zhao et al. 2023).

In October 2022, the CHIME/FRB collaboration reported a new FRB, named FRB 20220912A (McKinven & Chime/Frb

Collaboration 2022). Over the course of 3 days, nine bursts were detected in the CHIME band, leading to the expectation that this may become a highly active repeating FRB. According to McKinven & Chime/Frb Collaboration (2022), the dispersion measure (DM) of FRB 20220912A is $\sim$220 pc cm^{-3}, with a small RM value of 0.6 rad m^{-2}. The high activity level of FRB 20220912A allowed the DSA-110 collaboration to quickly localize the source in a host galaxy with a redshift of 0.077 (Ravi et al. 2023). It is speculated that this host galaxy contributes less than 50 pc cm^{-3} to DM, considering a Galactic DM contribution of 125 pc cm^{-3} (Cordes & Lazio 2002) or 122 pc cm^{-3} (Yao et al. 2017), plus a Milky Way halo contribution of 10 pc cm^{-3} (Keating 2020). The low host-galaxy DM contribution is in contrast to the host galaxies of FRB 20121102A and FRB 20190520B, which contribute a significant amount of DM (Chatterjee et al. 2017; Niu et al. 2022). Since FRB 20220912A's discovery, numerous telescopes and telescope arrays have detected bursts from FRB 20220912A (Bhusare et al. 2022; Fedorova & Rodin 2022; Herrmann 2022; Kirsten et al. 2022a; Ould-Boukattine et al. 2022; Pelliciari et al. 2022; Perera et al. 2022; Rajwade et al. 2022; Ravi 2022; Sheikh et al. 2022; Yu et al. 2022; Zhang et al. 2022a; Feng et al. 2023), attesting to its high brightness and activity.

Here, we report on the Five-hundred-meter Aperture Spherical radio Telescope (FAST) observation of the active, repeating FRB 20220912A. Our observations and data processing procedures are described in Section 2. Our results are presented in Section 3. We discuss the circular polarization expressions in Section 4 and conclude in Section 5.

2. Observations and Data Processing

FRB 20220912A has been observed since October 28th, 2022, using the center beam of the FAST 19 beam receiver (Dunning et al. 2017) pointing to the coordinate of R.A. = $23^{\rm h}09^{\rm m}04\overset{\rm s}{.}9$, decl. = $+48°42'25\overset{''}{.}4$ reported by DSA-110 (Ravi et al. 2023). In 2022, 17 observations with a total of 8.67 hr exposure time were carried out. A high-cadence calibration signal was periodically injected during the first minute of observation for the subsequent flux and polarization calibration. The data were recorded in FITS format with a time resolution of 49.152 μs, covering the frequency bandwidth from 1 to 1.5 GHz with 4096 frequency channels.

We used the same pipeline in Zhang et al. (2022b) to perform offline burst searches. According to the CHIME report, the DM value of FRB 20220912A is $\sim$220 pc cm^{-3}. The data were de-dispersed using this DM and then identified by a binary classification model[17] to determine whether a burst existed in a data segment. Additionally, we employed PRESTO (Ransom 2001) to cross-verify the search results. A total of 1076 bursts were detected.

We estimated the flux density of each burst using the radiometer equation with system temperature $T_{\rm sys}$ and telescope gain G modeled as a function of the zenith angle and observation frequency in Jiang et al. (2020). The burst profile is the average flux density that goes over the full observation frequency band. The peak flux $S_{\rm peak}$ is the maximum value of the burst profile. The burst fluence F is computed by integrating the burst profile with respect to time, and the equivalent width is computed by dividing the fluence by the peak flux. The energy is calculated using the equation

$$E = 10^{39}{\rm erg}\frac{4\pi}{1+z}\left(\frac{D_L}{10^{28}{\rm cm}}\right)^2\left(\frac{F}{{\rm Jy}\cdot{\rm ms}}\right)\left(\frac{\Delta\nu}{\rm GHz}\right), \quad (1)$$

where F is the fluence obtained and $\Delta\nu = 500$ MHz is the observation bandwidth. $D_L = 360.86$ Mpc is the luminosity distance of FRB 20220912A corresponding to the redshift $z = 0.0771$ (Ravi et al. 2023) adopting the standard Planck cosmological model (Planck Collaboration et al. 2016).[18]

Polarization calibration was achieved by correcting for the differential gain and phase between the receptors through separate measurements of a noise diode signal injected at an angle of 45° from the linear receptors with the single-axis model using the PSRCHIVE software package.

3. Results

3.1. Burst Rate and Time-series Analysis

Figure 1(F) displays the length of each observation, along with the number of detected bursts and event rates. Over the course of 17 observations, we detected a total of 1076 bursts, details of which can be found in Table 1. The event rates of eight observations exceeded 100 hr^{-1}, with the highest event rate of 390 hr^{-1} during the first observation, which is only surpassed by FRB20201124A's 542 hr^{-1} (Zhang et al. 2022b), demonstrating that FRB 20220912A is a highly active repeating FRB.

We calculated the waiting times between bursts for each observation. Similar to FRB 20121102A and FRB 20201124A, FRB 20220912A also exhibits a distinctive bimodal distribution (Figure 2). We utilized two lognormal functions to model the waiting-time distribution, with peaks located around 18 s and 51 ms, respectively.

The waiting times of a Poisson process are exponentially distributed. Here, we use an exponential function to fit the waiting-time distribution using the waiting times down to the second valley of the two lognormal distribution ($\sim$0.52 s). We utilize a Kolmogorov–Smirnov (K-S) test to evaluate the goodness of the lognormal and exponential fits, with p-values of 0.969 and 0.963, respectively, indicating that both models effectively describe the distribution. The Poisson process rate obtained from the exponential distribution is 0.041 ± 0.002 s^{-1} or 147 ± 7 hr^{-1}, which is close to the average observed event rate of $1076/8.67 \sim 124$ hr^{-1}. The right peak of the waiting time represents the activity of the FRB source during the statistical period. The lognormal provides a left peak of the waiting time near 51 ms, which is quite similar to FRB 20201124A (39 ms in Xu et al. 2022 and 51 ms in Zhang et al. 2022b). The left peak of FRB 20121102A is about 3 ms (Li et al. 2021), significantly different from FRB 20220912A here. However, FRB 20121102A appears to have a weak secondary peak around 51 ms (Figure 3 in Li et al. 2021). The characteristic waiting time of 51 ms may signify some fundamental properties of the FRB source emitting the bursts.

[17] https://github.com/SukiYume/DRAFTS

[18] The calculation of an FRB isotropic energy depends on the spectral shape of the burst (see Zhang 2022a for a discussion). If the spectrum is wide (power law–like), it is more appropriate to use the central frequency rather than bandwidth to estimate the energy. If the spectrum is narrow, especially with a measurable width within the telescope bandpass, it is more appropriate to use the bandwidth in the calculation. The repeating bursts typically have narrow spectra, so it is more appropriate to use Equation (1) to perform the calculations.

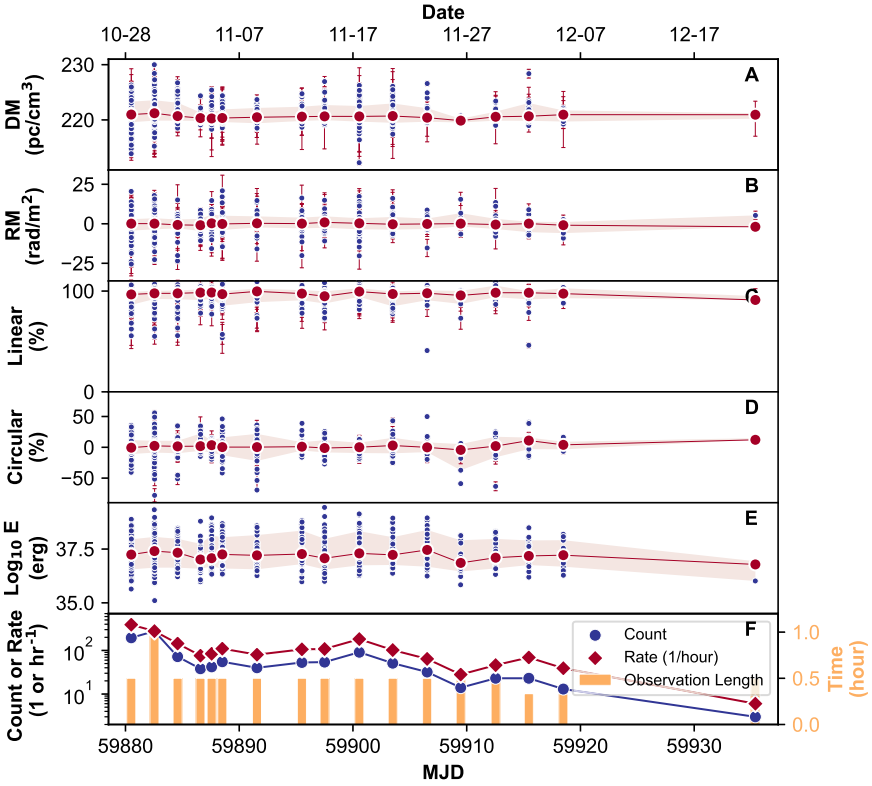

Figure 1. The properties of the bursts from FRB 20220912A observed by FAST. (A), (B), (C), (D), and (E) respectively denote the DM, RM, linear polarization, circular polarization, and energy of the bursts. Each burst is depicted by a blue point with error bars, the red points represent the daily median, and the light red area encompasses the 1σ range. (F) displays the number of bursts detected (blue) and the event rate (red), while the yellow bar symbolizes the observation length.

Searching for periodicity of FRBs remains an active research area. There have been three non-repeating FRBs discovered to have millisecond-level quasi-periods (Chime/Frb Collaboration et al. 2022). For repeating FRBs, however, no reports of short periods have emerged (Zhang et al. 2018; Li et al. 2021; Niu et al. 2022; Xu et al. 2022). Here, we also conducted a period search for FRB 20220912A using two methods: Lomb–Scargle periodograms (LSPs) and phase folding. The LSP method has been widely applied to nonuniformly sampled time series (Lomb 1976; Scargle 1982), making it suitable for periodic searches in the arrival time series of FRBs. Phase folding is also a simple and foundational method for period searches. Here, we assumed MJD 59,880 as the initial phase and computed the phase of each burst under a preset period, counting the longest continuous phase interval without burst existence, i.e., the void fraction. We iterated over periods ranging from 1 ms to 1000 s and computed the void fraction under these periods. A larger void fraction means a more concentrated burst distribution in the phase space, indicating higher reliability of the corresponding period. This approach is similar to the statistics used in Rajwade et al. (2020), except that we directly calculate the phase of the burst, making it more efficient and accurate. Unfortunately, neither of these two methods yielded a valid periodicity in the burst arrival times.

Only FRB 20121102A and FRB 20180916B have been reported to possess potential periodicities, the former approximately 157 days (Rajwade et al. 2020; Cruces et al. 2021), the latter approximately 16 days (Chime/Frb Collaboration et al. 2020). These periodicities are composed of active and quiescent phases (like square waves), and not all active phases had burst detection. Bursts from FRB 20220912A have been detected in all of our observations, precluding exploration of such active-quiescent periods. However, we can define the event rate variations over time as a "light curve" to search for possible periodicities in activity levels. Given the 54 days duration of FAST observations, we can only search for periodicities up to 27 days. To avoid observational interference on a 1 day period, we commence our search from a 2 day period. Utilizing LSPs, no reliable periodicities were found within the period range of 2 and 27 days.

3.2. Energy

Energy is one of the basic properties of FRBs, which is a physical quantity that can directly reflect the radiation mechanism of FRBs. The energy function of FRBs is typically modeled as a power-law function, probably with a cutoff at the high end (e.g., Luo et al. 2018; Lu et al. 2020; Luo et al. 2020; Zhang et al. 2021). Li et al. (2021)'s detection of the low-energy outburst of FRB 20121102A reveals the multiple radiation mechanisms that FRBs may possess. Figure 3 displays the energy function of FRB 20220912A, along with its distribution over time. Due to varying observation lengths, the energy function is weighted based on the observation time. Like FRB 20121102A and FRB 20201124A (Aggarwal et al. 2021; Li et al. 2021; Xu et al. 2022; Zhang et al. 2022b; Jahns et al. 2023), the differential energy function of FRB 20220912A cannot be explained using one single function. Two lognormal functions are used for the fit, with the corresponding characteristic energies being 5.29×10^{36} erg and 4.13×10^{37} erg, respectively. The integral energy function also cannot be fit with a single power law. Two sections of power-

Table 1
The Properties of the FRB 20220912A Bursts

Burst ID	MJD[a]	DM ($pc\ cm^{-3}$)	Peak Flux[b] (mJy)	Width[c] (ms)	Peak Frequency[d] (MHz)	Bandwidth[e] (MHz)	Fluence[b] (Jy ms)	Energy (erg)	RM ($rad\ m^{-2}$)	Linear (%)	Circular (%)
B01	59,880.497624400	220.24 ± 1.76	117.4 ± 1.4	4.70	1479.5 ± 5.4	122.4 ± 9.3	0.552 ± 0.007	3.979(49)e+37	$-4.3^{+2.1}_{-1.9}$	95.0 ± 1.4	5.3 ± 1.0
B02	59,880.497624673	217.82 ± 2.9	115.5 ± 1.4	3.72	1366.2 ± 4.3	231.4 ± 15.0	0.429 ± 0.005	3.097(38)e+37	$-0.3^{+0.8}_{-0.8}$	98.5 ± 1.8	-16.9 ± 1.3
B03	59,880.497684224	221.87 ± 0.06	242.8 ± 3.0	4.09	1300.0 ± 13.7	735.7 ± 896.2	0.993 ± 0.012	7.161(88)e+37	$1.1^{+0.2}_{-0.2}$	97.7 ± 1.0	3.3 ± 0.7
B04	59,880.497945389	220.88 ± 3.78	174.6 ± 2.1	3.54	1381.0 ± 6.8	321.4 ± 28.0	0.619 ± 0.008	4.463(55)e+37	$0.5^{+0.5}_{-0.5}$	98.6 ± 1.4	-6.7 ± 1.0
B05	59,880.497991706	220.91 ± 0.24	32.1 ± 0.4	4.06	1095.7 ± 11.2	251.7 ± 34.6	0.130 ± 0.002	9.398(115)e+36	$-3.1^{+1.5}_{-1.8}$	94.5 ± 6.7	-16.1 ± 4.9
B06	59,880.498128495	219.64 ± 5.08	95.2 ± 1.2	4.89	1564.0 ± 56.7	338.4 ± 65.8	0.465 ± 0.006	3.355(41)e+37	$2.1^{+1.2}_{-1.2}$	90.6 ± 1.6	7.2 ± 1.2
B07	59,880.498199601	223.30 ± 0.17	138.2 ± 1.7	8.97	1449.5 ± 26.3	332.1 ± 63.9	1.240 ± 0.015	8.942(109)e+37	$0.1^{+0.4}_{-0.3}$	97.2 ± 0.9	14.8 ± 0.6
B08	59,880.498605364	222.98 ± 1.36	96.5 ± 1.2	8.65	1399.0 ± 15.2	374.2 ± 61.9	0.834 ± 0.01	6.019(73)e+37	$3.1^{+0.6}_{-0.6}$	97.8 ± 1.5	-2.7 ± 1.0
B09	59,880.498635029	220.22 ± 0.24	34.5 ± 0.4	0.64	1004.4 ± 22.4	110.3 ± 34.3	0.022 ± 0.0	1.592(19)e+36	...	...	...
B10	59,880.498915641	221.35 ± 0.21	77.7 ± 0.9	8.74	1083.0 ± 5.5	256.5 ± 16.1	0.679 ± 0.008	4.898(59)e+37	$1.9^{+0.6}_{-0.6}$	98.7 ± 2.2	-3.8 ± 1.6

Notes. The full table is available in ScienceDB, doi:10.57760/sciencedb.08058.
[a] Barycentrical arrival time at 1.5 GHz.
[b] Calculated within 500 MHz bandwidth.
[c] Equivalent width.
[d] Obtained with Gaussian fitting.
[e] FWHM of Gaussian fitting.

(This table is available in its entirety in machine-readable form.)

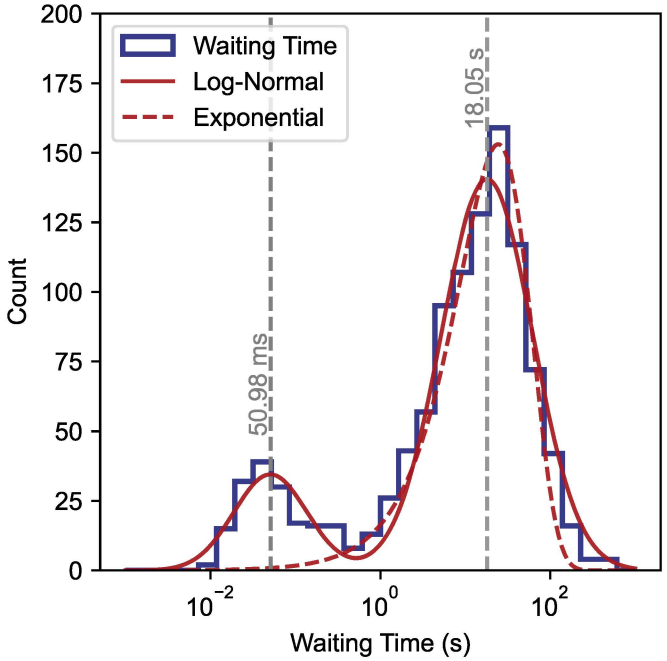

Figure 2. The waiting-time distribution of FRB 20220912A. The red solid line represents the best-fit model with two lognormal functions, and the red dashed line indicates the best-fit model with a single exponential function.

law fit are utilized, with the power-law exponents being -0.38 ± 0.02 and -2.07 ± 0.07. In Figure 3(C), the energy appears to exhibit an evolutionary characteristic over time, with fewer high-energy bursts observed in the latter observations.

After calibrating the time-frequency data, we calculate the fluence of each burst by integrating the flux with respect to time in each frequency channel. Then we average the fluence of all bursts to obtain the synthetic fluence-frequency spectrum of FRB 20220912A. As the different frequency channels of these bursts may be masked as radio frequency interference (RFI) channels, the number of bursts used for averaging fluence varies in frequency channels. We use Poisson counting error as the statistical error and use a simple power-law function to fit the spectral index of the synthetic spectrum:

$$I = A \times F^{\alpha} + C \tag{2}$$

In Figure 4 one can see large error bars near 1000, 1200 MHz, etc. due to frequent RFI interference, resulting in fewer effective data points. For the fit, we randomly select 90% of the data points from the available data and perform 1000 fits, resulting in the expectation and error of the FRB 20220912A spectral index being $\alpha = -2.60 \pm 0.21$. This is the first measurement of the average spectral index of the synthetic spectrum of an FRB source. Such a spectrum can, in principle, be used to test against FRB radiation mechanisms (e.g., curvature radiation; Yang & Zhang 2018).

Although the synthetic spectrum of all bursts conforms well to a power-law distribution, it is difficult to describe the relatively narrow bandwidth of individual bursts using a power-law model. Based on the current empirical evidence, a Gaussian function may be a viable alternative to describe the spectra of individual bursts. Prior research has employed a Gaussian model to investigate FRB 20121102A, with the fitting residual demonstrating the potential efficacy of the Gaussian distribution as a model, as illustrated in Figure 5 of Aggarwal et al. (2021). Similarly, Zhou et al. (2022) fitted the spectrum of

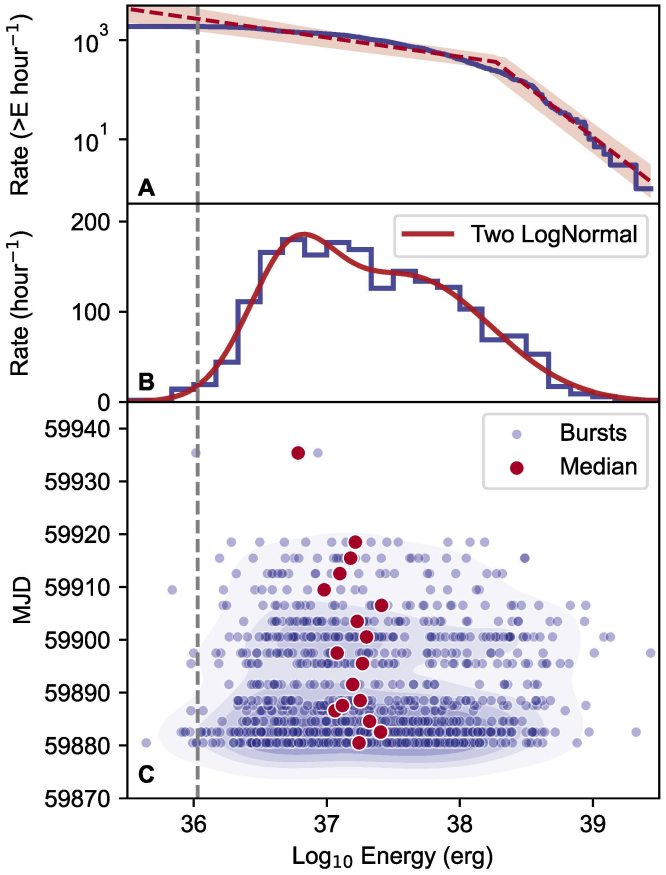

Figure 3. Energy distribution of FRB 20220912A. (A) The blue step represents the cumulative probability distribution of the energy function, while the red dashed line denotes the best-fit using a broken power-law function. The red region indicates the 1σ range of the fitting. (B) The differential probability distribution of the energy function, with the red line showing the fitting using two lognormal functions. (C) The time-dependent burst energy distribution. The blue dots display the energy of 1076 bursts; red dots denote the median energy; and the blue contours depict a 2D kernel density estimation (KDE) of the bursts. The gray dashed line represents the 90% detection threshold.

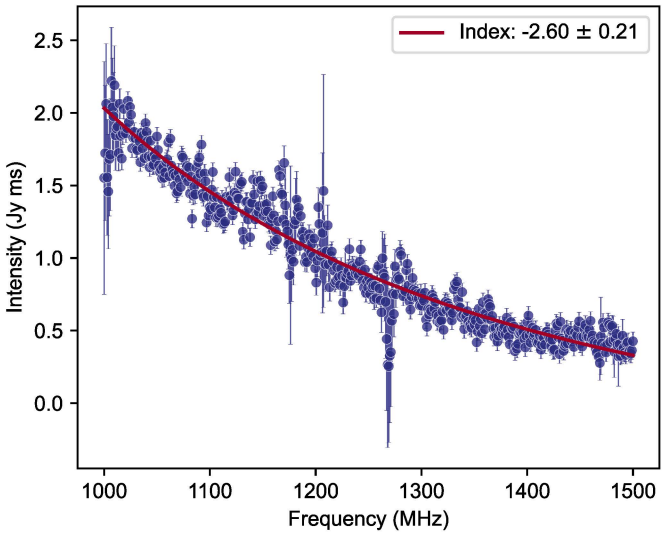

Figure 4. Power-law fitting (red line) to the synthetic spectrum of FRB 20220912A.

FRB 20201124A with Gaussian functions and identified a bimodal distribution of central frequencies. Here, we also attempt to fit the spectrum of individual bursts using a Gaussian

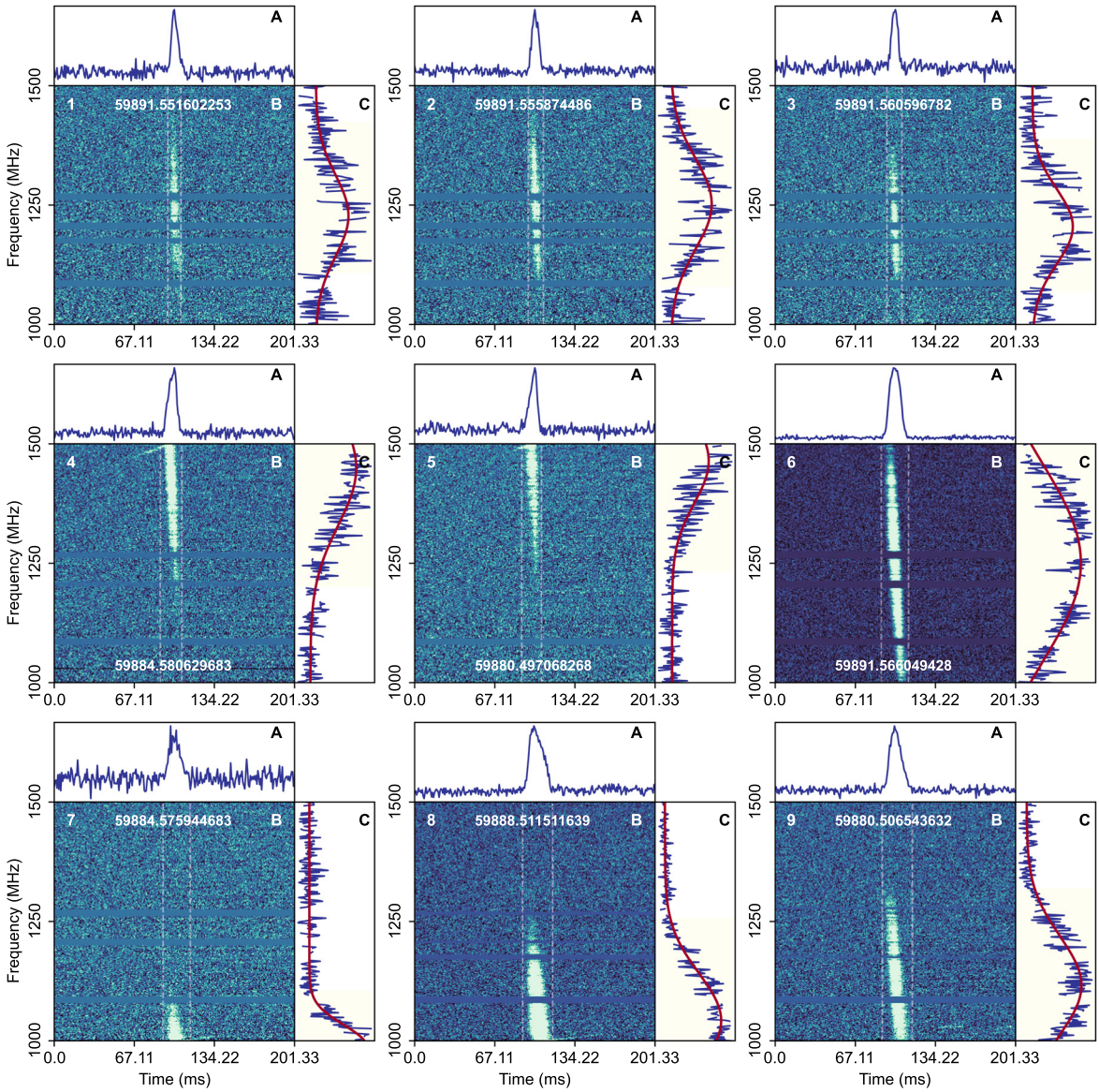

Figure 5. Bandwidth fitting examples of the FRB 20220912A bursts.

function:

$$I = A \times \exp\left[-\frac{(F-\mu)^2}{2\sigma^2}\right], \quad (3)$$

where we use the fitted μ as the center frequency ν_0 and FWHM ($2\sqrt{2\ln 2}\,\sigma$) as the bandwidth $\Delta\nu$. It should be noted that due to the limited bandwidth of FAST, some bursts likely have emission outside the FAST band not fully recorded. This introduces additional uncertainties to the bandwidth fitting results. Nine examples of bandwidth fitting are illustrated in Figure 5.

Figure 6 presents the distribution of the central frequency (ν_0) and bandwidth ($\Delta\nu$) of the FRB 20220912A bursts. In order to mitigate the biases introduced by the limitations of observational bandwidth, we excluded bursts with ν_0 falling outside the range of 1–1.5 GHz and bursts with ν_0 within 50 MHz of the bandwidth edges (1 and 1.5 GHz) with bandwidth $\Delta\nu < 100$ MHz as these bursts are associated with high levels of fitting uncertainty. We subsequently analyzed the distribution of ν_0 and $\Delta\nu$ for the remaining bursts. The central frequency of FRB 20220912A bursts mainly concentrates on the low-frequency range, and the distribution of high and low frequencies is extremely uneven. We use a single lognormal function to fit the bandwidth distribution. The mode of the lognormal function is located at 181 MHz, indicating that FRB 20220912A's bursts have very narrowband spectra. Furthermore, we did not find significant correlation between central frequency and emission bandwidth according to the sample we collected at the *L*-band. This is different from the power-law trend found by Kumar et al. (2023) from the bursts detected by the Parkes ultra-wideband lower receiver from the repeater FRB 20180301A, which might imply the actual observed bandwidth matters for this kind of analysis.

A more relevant parameter to describe the narrowness of an FRB spectrum is $\Delta\nu/\nu_0$. We investigate $\Delta\nu/\nu_0$ in more detail. Because many bursts have emission outside of the FAST band (1–1.5 GHz), we limit our analysis to the bursts whose emission

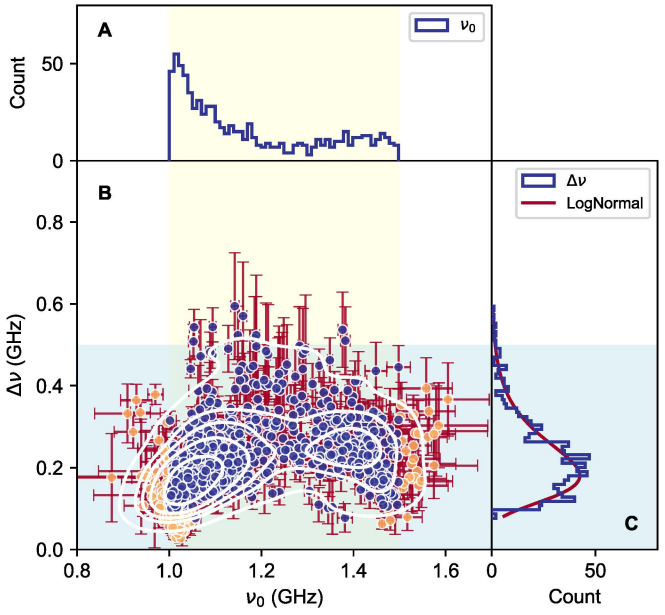

Figure 6. Distribution of the center frequency (ν_0) and spectral width ($\Delta\nu$) of the FRB 20220912A bursts fitted by Gaussian functions. The blue dots and lines in the figure represent bursts with peak frequency falling within the range of 1–1.5 GHz, and the fitting bandwidth exceeds 100 MHz when the peak frequency is below 1.05 GHz or above 1.45 GHz. The orange dots correspond to bursts that do not meet these conditions. (A) The distribution of the center frequency. (B) The scatterplot of the center frequency and spectral width. The white contours show the 2D KDE illustrating the spatial distribution of the center frequency and spectral width. The light yellow and light blue backgrounds indicate the observed (1–1.5 GHz) and effective (0.5 GHz) bandwidths of the FAST telescope, respectively. (C) The spectral width distribution fitted by a lognormal function with a peak value at 181 MHz.

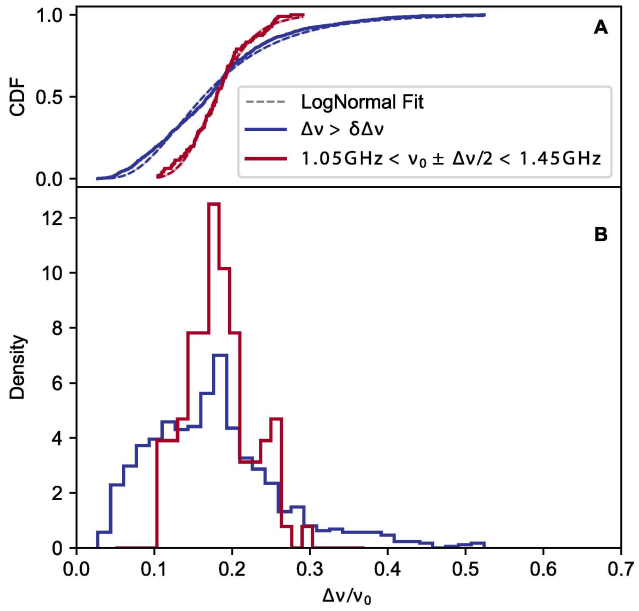

Figure 7. The $\Delta\nu/\nu_0$ distribution of FRB 20220912A. (A) The cumulative distribution function of $\Delta\nu/\nu_0$. (B) The differential probability distribution of $\Delta\nu/\nu_0$. For both panels, the blue lines and red lines are defined under two filtering criteria, i.e., the Gaussian fit standard deviation error $\delta\sigma$ is smaller than the standard deviation σ itself (blue), and FWHM of the burst spectrum is completely within the range of 1.05–1.45 GHz (red).

completely falls within the FAST band to avoid the bandwidth-selection effect. We select bursts based on two stringent criteria, i.e., the Gaussian fit standard deviation error $\delta\sigma$ is smaller than the standard deviation σ itself, and the FWHM of the burst spectrum is completely within the range of 1.05–1.45 GHz. Figure 7 displays the distribution $\delta\nu/\nu_0$ of these bursts under these two filtering criteria. We fit the histogram distributions using lognormal functions and obtain $\mu = -1.812 \pm 0.001$ and $\sigma = 0.475 \pm 0.002$ for the blue histogram and $\mu = -1.718 \pm 0.002$ and $\sigma = 0.217 \pm 0.003$ for the red histogram, respectively. From the fitting results, we obtain their modes $e^{\mu-\sigma^2}$ located at 0.13 and 0.17, respectively. We also fit the cumulative $\Delta\nu/\nu_0$ distribution using a power-law function. The results are suboptimal with significant fitting errors.

3.3. DM and Polarimetry

The DM of each burst was determined using the DM phase software package (Seymour et al. 2019),[19] which maximizes the coherent power in the pulse across the emission bandwidth. The median value of the DM is 220.70 pc cm^{-3} with a standard deviation of 1.83 pc cm^{-3}, which is consistent with CHIME's measurement of ~220 pc cm^{-3} (McKinven & Chime/Frb Collaboration 2022). Linear fitting indicates the absence of any trend in the time evolution of DM, where the slope is dDM/dt $< 8 \times 10^{-3}$ pc cm^{-3} day^{-1}.

Due to the Faraday effect, the polarization plane of the FRB signal undergoes rotation during propagation. We employed the RM synthesis method to fit the RM of the burst using Equation (4),

$$\begin{pmatrix} I \\ Q' \\ U' \\ V \end{pmatrix} = \begin{bmatrix} 1 & 0 & 0 & 0 \\ 0 & \cos 2\theta & \sin 2\theta & 0 \\ 0 & -\sin 2\theta & \cos 2\theta & 0 \\ 0 & 0 & 0 & 1 \end{bmatrix} \begin{pmatrix} I \\ Q \\ U \\ V \end{pmatrix}, \quad (4)$$

where $\theta = \mathrm{RM}\lambda^2$. We selected bursts with RM errors less than 10 rad m^{-2} (881 in total) for presentation.

The mean value of the RM is -0.08 rad m^{-2}, close to 0, indicating that the RM contribution from FRB 20220912A's host galaxy is comparable to that of the Milky Way, which is about -16 rad m^{-2} (Hutschenreuter et al. 2022). The low value of RM indicates that the FRB 20220912A may be in a very clean environment. The linear fit also suggests that there is no trend in the evolution of RM with time, with a slope of 0.017 ± 0.018 day^{-1}. Furthermore, several other active repeating FRBs, such as FRB 20121102A (Hilmarsson et al. 2021a), 20201124A (Xu et al. 2022), 20190520B (Anna-Thomas et al. 2023), 20180916B (Mckinven et al. 2023a), and several other bursts (20181030A, 20181119A, 20190117A, 20190208A, 20190303A, 20190417A; Mckinven et al. 2023b) exhibit large RM values and show variations in RM on the timescale of months. In contrast to these repeating FRBs with large RMs, which suggest that all repeaters may have associated synchrotron-emitting persistent radio sources (a supernova remnant, a magnetar wind nebula or a mini-AGN) with a dense and highly magnetized environment, the polarization data of FRB 20220912A suggest that a large and varying RM is not the necessary condition to make active repeaters.

The linear polarization that is measured can be subject to overestimation when noise is present. As a result, we employ the frequency-averaged total linear polarization that has been

[19] https://github.com/danielemichilli/DM_phase

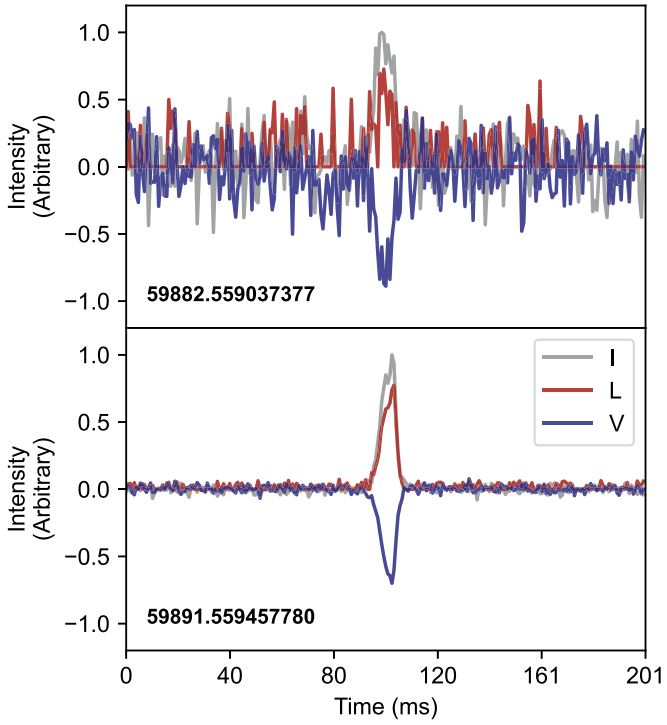

Figure 8. Two bursts with the highest circular polarization degrees. The black, red, and blue lines respectively represent the burst's total intensity, linear polarization, and circular polarization profiles.

de-biased (Everett & Weisberg 2001),

$$L_{\rm de-bias} = \begin{cases} \sigma_I \sqrt{\left(\frac{L_i}{\sigma_I}\right)^2 - 1} & \frac{L_i}{\sigma_I} > 1.57 \\ 0 & \frac{L_i}{\sigma_I} \leqslant 1.57 \end{cases}, \quad (5)$$

where σ_I represents the off-pulse standard deviation of Stokes I, while L_i is the frequency-averaged linear polarization that has been measured for time sample i. The degree of linear and circular polarization are calculated with

$$L = \frac{\sum_i L_{\rm de-bias,i}}{\sum_i I_i} \quad \text{and} \quad V = \frac{\sum_i V_i}{\sum_i I_i}, \quad (6)$$

where V_i is defined similarly to L_i. The uncertainties on the linear polarization fraction and circular polarization fraction are calculated as

$$\sigma = \frac{\sigma_I}{I}\sqrt{N + N(\rho^2/I^2)}, \quad (7)$$

where N is the number of time samples of the burst and ρ is $\sum_i L_{\rm de\text{-}bias,i}$ or $\sum_i V_i$, depending on whether we are calculating the linear or circular polarization fraction.

Most of the bursts from FRB 20220912A exhibit almost 100% linear polarization, with a noticeable fraction of bursts exhibiting significant circular polarization. Figure 8 displays the two bursts with the highest circular polarization degrees, which are $-78.0\% \pm 10.8\%$ and $-69.4\% \pm 1.4\%$, respectively.

Additionally, the circular polarization dynamic spectra of FRB 20220912A show various morphologies. We display 16 bursts in Figure 9. It can be seen that some bursts that cannot be distinguished in Stokes I appear as multiple bursts in Stokes V, such as bursts 1, 2, 7, 11, and 16. The bursts that show sign changes in circular polarization also have sub-pulse structures, so that the sign change may be caused by sub-pulses with different circular polarization modes at different times. The mechanism responsible for circular polarization is still under extensive discussion and no definitive conclusion has been reached (Qu & Zhang 2023). Curvature radiation by emitting bunches can be circularly polarized if the line of sight (LOS) is not confined in a beaming angle (Wang et al. 2022c). A sign change of circular polarization can be seen if the opening angle of the bunch is not much larger than $1/\gamma$, where γ is the Lorentz factor of the bunch (Wang et al. 2022b). The curvature radiation mechanism predicts an average circular polarization fraction smaller than 55% when a sign change of circular polarization occurs. Another intrinsic radiation mechanism is the coherent inverse Compton scattering through charged bunches (Zhang 2022b; Qu et al. 2023). The scattered waves can be circularly polarized by adding up linearly polarized waves with different phases and polarization angles (Qu & Zhang 2023). When the LOS sweeps across the bunch's central axis, the sign of circular polarization can change, and the maximum circular polarization fraction can be larger than that of curvature radiation. The observation of FRB 20220912A could be understood within either scenario.

Circular polarization in some bursts also appears to vary with frequency (Figure 10). An oscillation of polarization parameters as a function of wavelength may be an indication of Faraday conversion (Xu et al. 2022; Qu & Zhang 2023). However, the polarization degree of FRB 20220912A oscillates without an obvious oscillation frequency like FRB 20201124A (Xu et al. 2022). Furthermore, the conditions for significant Faraday conversion are usually quite stringent (Qu & Zhang 2023), requiring special magnetic field reversal environments, e.g., in a binary star system (Wang et al. 2022a) or when the source is surrounded by a supernova remnant (Yang et al. 2023). Such a required environment is not consistent with the very clean environment inferred from the small and non-variable RM of FRB 20220912A.

4. Discussion

4.1. Total Energy Budget

By utilizing the isotropic energies derived from each burst, it is possible to impose limitations on the total energy allocation of the intrinsic FRB source, which can be employed to restrict the various models of FRB sources. When deducing the total source energy based on the energy of each burst, various factors must be considered, including radio radiation efficiency η_r, beaming factor f_b, and observation duty cycle ζ (Zhang 2022a).

We use Equation (1) for energy calculation with the isotropic emission assumption. However, coherent radiation from FRB bursts generally has a small solid angle $\delta\Omega$. Therefore, the true burst energy should be $\delta\Omega/4\pi$ of the isotropic burst energy. Additionally, bursts may exist in directions that are not observable. Assuming the global emission beam to be $\Delta\Omega$, we can get the global beaming factor $f_b = \Delta\Omega/4\pi$.

Due to the limitation of the observation duty cycle, we cannot observe all bursts emitted by the FRB source during the observation period. For example, our observations of FRB 20220912A were conducted over 17 days with a total observation time of only 8.67 hr, which does not imply that

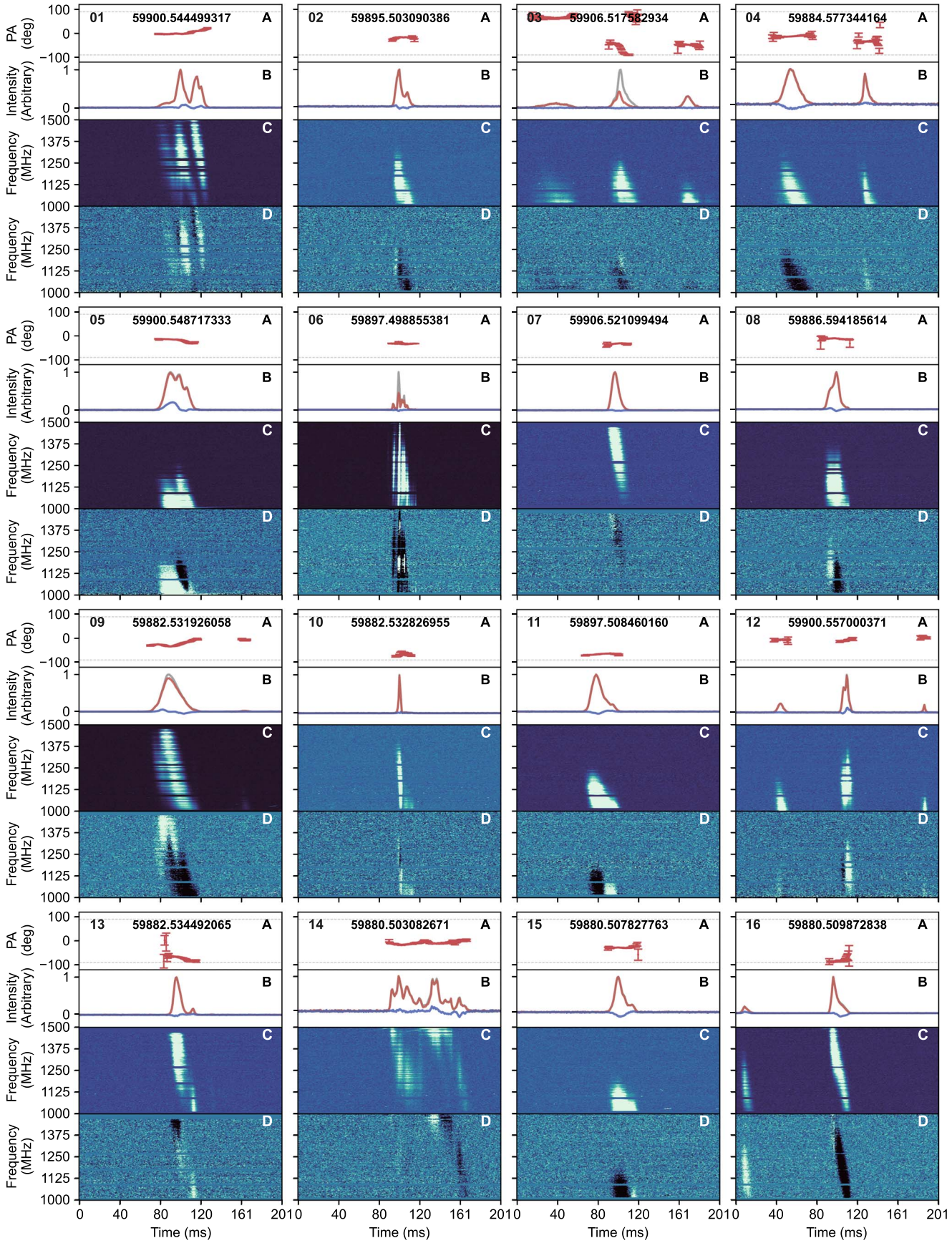

Figure 9. Sixteen bright bursts from FRB 20220912A with circular polarization reversal over time or/and frequency. (A) Polarization position angle (PA). (B) Polarization profiles of the bursts, with the black, red, and blue lines representing the total intensity, linear polarization, and circular polarization, respectively. (C) Stokes I. (D) Stokes V.

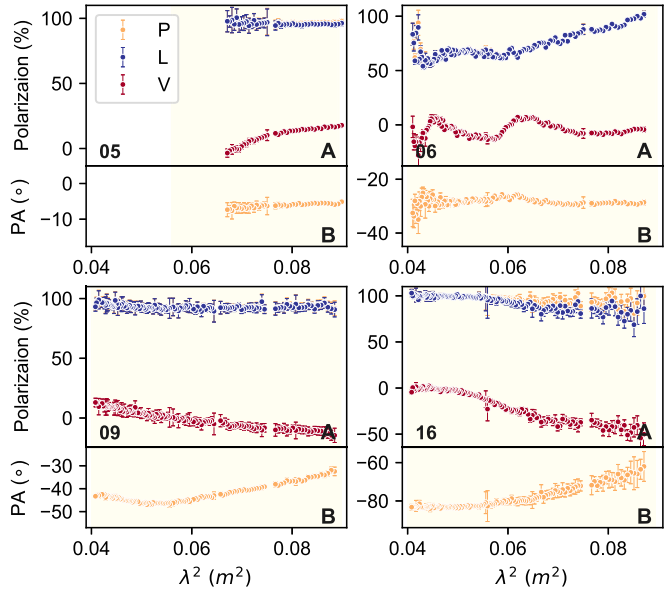

Figure 10. Four bright bursts from FRB 20220912A with circular polarization oscillating over frequency. (A) Polarization degree. (B) PA.

there was no activity at other hours. Therefore, to estimate the total source energy during the observation period, we can use duty-cycle scaling to compensate for the unobserved periods of FRB radiation energy. If the total radio energy of the observed bursts is E_b, the total source energy should be $E_b \times f_b \times \eta_r^{-1} \times \zeta^{-1}$.

Table 2 presents our estimates of the total source energy for FRB 20121102A (Li et al. 2021), FRB 20190520B (Niu et al. 2022), FRB 20201124A (Xu et al. 2022; Zhang et al. 2022b), and FRB 20220912A (this paper) using FAST observations. In our calculations, we assumed typical values for η_r and f_b of 10^{-4} and 0.1, respectively. It should be noted that the burst energies reported in the literature for FRB 20121102A and FRB 20190520B were calculated using a center frequency of 1.25 GHz, rather than the bandwidth $\Delta\nu$. Therefore, we have divided the total energies of these two FRBs by 2.5 to allow for comparison with the other FRBs (see footnote 18 for more discussion). FRB 20220912A emitted an energy of 3.49×10^{45} erg during the 17 day period, which exceeds 2% of the total dipolar magnetic energy ($E_B \sim 1.7 \times 10^{47}$ erg) of a magnetar. This implies that the dipolar magnetic energy of the magnetar would be completely depleted in only ~850 days if the radio efficiency is indeed as low as 10^{-4}. Certain magnetar models (e.g., low-efficiency models invoking relativistic shocks) would suffer from an energy budget problem.

4.2. Circular Polarization and Environment

FRB 20201124A was the first repeating FRB discovered with circular polarization (Hilmarsson et al. 2021b). Prior to this, only some non-repeating bursts were found to have significant circular polarization (Cho et al. 2020; Day et al. 2020; Feng et al. 2022a). Recently, FRB 20121102A and FRB 20190520B were detected by FAST with very few bursts exhibiting circular polarization (Feng et al. 2022b). Here, we present that FRB 20220912A has a large number of bursts exhibiting circular polarization, suggesting that this may be a common feature of repeating FRBs.

Table 2
Energy Budget of Four Repeating FRBs

FRB Name	Duty Cycle[a] ζ	Radio E[b] (erg)	Averaged E[c] (erg hr^{-1})	Source E[d] ($\eta_{r,-4}^{-1} f_{b,-1}$ erg)[e]
20121102A	0.053	1.36×10^{41}	2.29×10^{39}	2.59×10^{45}
20190520B	0.070	4.39×10^{39}	2.37×10^{38}	6.26×10^{43}
20201124A[f]	0.063	1.65×10^{41}	2.01×10^{39}	2.60×10^{45}
20201124A[g]	0.042	6.42×10^{40}	1.60×10^{40}	1.54×10^{45}
20220912A	0.021	7.42×10^{40}	8.55×10^{39}	3.49×10^{45}

Notes.
[a] The observation duty cycle, e.g., for FRB 20220912A in this paper, the duty cycle is 8.67 hr out of 17 days.
[b] Sum of the observed isotropic radio energies of all bursts.
[c] The total radio energy divided by observation time, e.g., for FRB 20220912A in this paper, the averaged energy is 7.42×10^{40} erg/8.67 hr.
[d] The total source energy.
[e] The source energy calculation uses $\eta_r = 10^{-4}$ and $f_b = 0.1$.
[f] FAST observation of FRB 20201124A in 2021.04 by Xu et al. (2022).
[g] FAST observation of FRB 20201124A in 2021.09 by Zhang et al. (2022b).

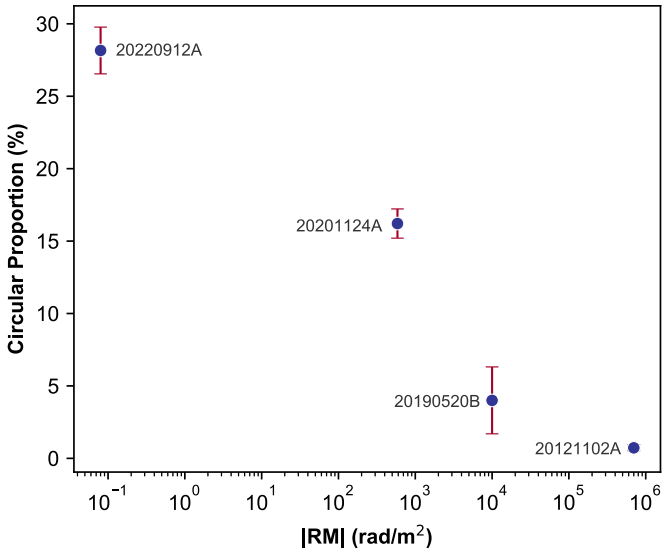

Figure 11. The proportion of bursts with circular polarization from repeating FRBs varies with RM. The red error bars are given by the Poisson counting error of the statistical counts. The error bar on FRB 20121102A is smaller than the symbol size.

All the above-mentioned four repeating FRBs have a large number of detected bursts by FAST. We counted the proportion of bursts exhibiting significant circular polarization (circular degree $\geqslant$10%) for each of these four repeating FRBs. FRB 20121102A exhibited 12 out of 1652 detected bursts with circular polarization (Li et al. 2021; Feng et al. 2022b). Similarly, FRB 20190520B displayed circular polarization in 3 out of 75 detected bursts (Feng et al. 2022b; Niu et al. 2022). FRB 20201124 showed circular polarization in 302 out of 1863 detected bursts (Xu et al. 2022), while FRB 20220912A exhibited circular polarization in 303 out of 1076 detected bursts (this paper).

Figure 11 shows a tentative relationship between the fraction of bursts with circular polarization degree >10% and the absolute value of each FRB's RM. It appears that there is a negative correlation. The larger the RM value, the lower the fraction of bursts with circular polarization. If such a correlation is physical, it may be related to the intrinsic radiation mechanism

and complicated environments of repeating FRB sources. First, the larger fraction of circular polarization in the clean-environment FRB 20121102A suggests that the origin of circular polarization may be more related to intrinsic radiation mechanisms than environment effects. According to Qu & Zhang (2023), significant circular polarization can be made from magnetospheric radiation mechanisms such as coherent curvature radiation or inverse Compton scattering by bunches. Relativistic shock models invoking synchrotron maser radiation mechanism, on the other hand, mostly emit bursts with nearly 100% linear polarization (Metzger et al. 2019; Plotnikov & Sironi 2019; Qu & Zhang 2023). The detection of circular polarization from all four sources favors the magnetospheric origin of the bursts. Second, in case of both curvature and inverse Compton scattering processes, given a random viewing angle, the fraction of bursts that have high circular polarization degree is high if the bunch shape is point-like. In order to reduce the fraction of circularly polarized bursts, the cross section of the bunches should be large so that most emitting leptons are viewed on beam (e.g., Wang et al. 2022b). The correlation seen in Figure 11 would then require that the FRB engine residing in a more magnetized environment (e.g., a younger magnetar) should be able to generate bunches with larger cross sections. Such a scenario may predict that the bursts from a more magnetized environment are systematically brighter, which is not observed. An alternative, possibly a more likely, scenario is that the circular polarization fraction is modified by environments. Qu & Zhang (2023) showed that polarization-mode-selected synchrotron absorption tends to convert circular polarization to linear polarization. The observed trend in Figure 11 then suggests that there is more significant synchrotron absorption in more magnetized environments. More repeater data are needed to confirm whether the circular polarization fraction and RM correlation is physical.

5. Conclusions

We report the observation of FRB 20220912A by FAST in 2022.

1. A total of 1076 bursts were detected, with the highest event rate of 390 hr^{-1}. No periodicity in the range of 1 ms–1000 s or 2–27 days was detected.
2. The energy distribution of FRB 20220912A cannot be described by a single function. The differential energy distribution was described using two lognormal functions, with characteristic energies 5.29×10^{36} erg and 4.13×10^{37} erg. The cumulative energy distribution was described using a broken power-law function, with power-law indices -0.38 ± 0.02 and -2.07 ± 0.07.
3. We report, for the first time, the synthetic spectrum of many bursts of FRB 20220912A. It can be fitted by a power-law function with an *L*-band spectral index of −2.6.
4. The RM of FRB 20220912A is close to 0 and did not show any evolution during the 2 month observation period, indicating that the contribution of the Milky Way and the host galaxy to RM is comparable. The contribution of the Milky Way is estimated to be $-16\ rad\ m^{-2}$, suggesting that FRB 20220912A is located in a relatively clean local environment. This FRB suggests that a high and variable RM is not the necessary condition for making an active FRB repeater.
5. Most bursts of FRB 20220912A in the *L*-band exhibit nearly 100% linear polarization, and a large fraction of the bursts exhibit circular polarization, with a maximum of 70%. Some of the bursts had their circular polarization changing sign over time or frequency. The high circular polarization degree of the bursts is likely related to the intrinsic radiation mechanisms. Likely models include coherent curvature radiation and inverse Compton scattering by bunches within the magnetosphere of the FRB source.
6. We found a tentative anticorrelation between |RM| and the circular polarization fraction, i.e., a larger |RM| corresponds to a smaller fraction of circularly polarized bursts. If such an anticorrelation is real, it may imply more mode-selected synchrotron absorption in more magnetized environments.

Multiwavelength observations of FRBs are essential to understanding their origins and environments. FRB 20220912A is located in a host galaxy with $z \sim 0.077$, making it the third-closest repeating FRBs after FRB 20200120E (Kirsten et al. 2022b) and FRB 20180916B (Marcote et al. 2020). Its proximity means that multiwavelength observations will be more efficient. Furthermore, FRB 20220912A is a very active repeating FRB, which makes it an ideal target for multiwavelength observations. We encourage further multiwavelength observations of FRB 20220912A to unravel the mystery of FRBs.

Acknowledgments

This work made use of the data from FAST, a Chinese national mega-science facility, operated by National Astronomical Observatories, Chinese Academy of Sciences. This work was supported by the National Natural Science Foundation of China (NSFC, grant Nos. 11988101, 12203045, 11725313, 12003028 and 12041303). This work was supported by the National SKA Program of China No. 2020SKA0120200 and 2022SKA0130100, the CAS-MPG LEGACY project, and YSBR-063, CAS Project for Young Scientists in Basic Research.

Data Availability

The full table for bursts' properties is in Table 1. The data underlying this paper will be shared on a reasonable request to the corresponding author.

ORCID iDs

Yong-Kun Zhang https://orcid.org/0000-0002-8744-3546
Di Li https://orcid.org/0000-0003-3010-7661
Yi Feng https://orcid.org/0000-0002-0475-7479
Wei-Yang Wang https://orcid.org/0000-0001-9036-8543
Wei-Wei Zhu https://orcid.org/0000-0001-5105-4058
Jin-Lin Han https://orcid.org/0000-0002-9274-3092
Peng Jiang https://orcid.org/0000-0002-5387-7952
Dong-Zi Li https://orcid.org/0000-0001-7931-0607
Rui Luo https://orcid.org/0000-0002-4300-121X
Chen-Hui Niu https://orcid.org/0000-0001-6651-7799
Pei Wang https://orcid.org/0000-0002-3386-7159
Fa-Yin Wang https://orcid.org/0000-0003-4157-7714
Yuan-Pei Yang https://orcid.org/0000-0001-6374-8313

References

Aggarwal, K., Agarwal, D., Lewis, E. F., et al. 2021, ApJ, 922, 115
Anna-Thomas, R., Connor, L., Dai, S., et al. 2023, Sci, 380, 599
Bhusare, Y., Kumar, A., Maan, Y., et al. 2022, ATel, 15806, 1
Chatterjee, S., Law, C. J., Wharton, R. S., et al. 2017, Natur, 541, 58

Chime/Frb Collaboration, Amiri, M., Andersen, B. C., et al. 2020, Natur, 582, 351
Chime/Frb Collaboration, Andersen, B. C., Bandura, K., et al. 2022, Natur, 607, 256
Cho, H., Macquart, J.-P., Shannon, R. M., et al. 2020, ApJL, 891, L38
Cordes, J. M., & Lazio, T. J. W. 2002, arXiv:astro-ph/0207156
Cruces, M., Spitler, L. G., Scholz, P., et al. 2021, MNRAS, 500, 448
Day, C. K., Deller, A. T., Shannon, R. M., et al. 2020, MNRAS, 497, 3335
Dunning, A., Bowen, M., Castillo, S., et al. 2017, Design and laboratory testing of the five hundred meter aperture spherical telescope (FAST) 19 beam L-band receiver, in 2017 XXXIInd General Assembly and Scientific Symp. Int. Union of Radio Science (URSI GASS) (Piscataway, NJ: IEEE) 1
Everett, J. E., & Weisberg, J. M. 2001, ApJ, 553, 341
Fedorova, V. A., & Rodin, A. E. 2022, ATel, 15713, 1
Feng, Y., Li, D., Yang, Y.-P., et al. 2022a, Sci, 375, 1266
Feng, Y., Li, D., Zhang, Y.-K., et al. 2023, arXiv:2304.14671
Feng, Y., Zhang, Y.-K., Li, D., et al. 2022b, SciBu, 67, 2398
Herrmann, W. 2022, ATel, 15691, 1
Hilmarsson, G. H., Michilli, D., Spitler, L. G., et al. 2021a, ApJL, 908, L10
Hilmarsson, G. H., Spitler, L. G., Main, R. A., & Li, D. Z. 2021b, MNRAS, 508, 5354
Hutschenreuter, S., Anderson, C. S., Betti, S., et al. 2022, A&A, 657, A43
Jahns, J. N., Spitler, L. G., Nimmo, K., et al. 2023, MNRAS, 519, 666
Jiang, P., Tang, N.-Y., Hou, L.-G., et al. 2020, RAA, 20, 064
Keating, L. C., & Pen, U.-L. 2020, MNRAS, 496, L106
Kirsten, F., Hessels, J. W. T., Hewitt, D. M., et al. 2022a, ATel, 15727, 1
Kirsten, F., Marcote, B., Nimmo, K., et al. 2022b, Natur, 602, 585
Kumar, P., Luo, R., Price, D. C., et al. 2023, arXiv:2304.01763
Li, D., Wang, P., Zhu, W. W., et al. 2021, Natur, 598, 267
Lomb, N. R. 1976, Ap&SS, 39, 447
Lorimer, D. R., Bailes, M., McLaughlin, M. A., Narkevic, D. J., & Crawford, F. 2007, Sci, 318, 777
Lu, W., Kumar, P., & Zhang, B. 2020, MNRAS, 498, 1397
Luo, R., Lee, K., Lorimer, D. R., & Zhang, B. 2018, MNRAS, 481, 2320
Luo, R., Men, Y., Lee, K., et al. 2020, MNRAS, 494, 665
Marcote, B., Nimmo, K., Hessels, J. W. T., et al. 2020, Natur, 577, 190
McKinven, R. & Chime/Frb Collaboration 2022, ATel, 15679, 1
Mckinven, R., Gaensler, B. M., Michilli, D., et al. 2023a, ApJ, 950, 12
Mckinven, R., Gaensler, B. M., Michilli, D., et al. 2023b, ApJ, 951, 82
Metzger, B. D., Margalit, B., & Sironi, L. 2019, MNRAS, 485, 4091
Michilli, D., Seymour, A., Hessels, J. W. T., et al. 2018, Natur, 553, 182
Nimmo, K., Hessels, J. W. T., Snelders, M. P., et al. 2023, MNRAS, 520, 2281
Niu, C. H., Aggarwal, K., Li, D., et al. 2022, Natur, 606, 873
Ould-Boukattine, O. S., Herrmann, W., Gawronski, M., et al. 2022, ATel, 15817, 1
Pelliciari, D., Bernardi, G., Pilia, M., et al. 2022, ATel, 15695, 1
Perera, B., Perillat, P., Fernandez, F., et al. 2022, ATel, 15734, 1
Planck Collaboration, Ade, P. A. R., & Aghanim, N. 2016, A&A, 594, A13
Plotnikov, I., & Sironi, L. 2019, MNRAS, 485, 3816
Qu, Y., & Zhang, B. 2023, MNRAS, 522, 2448
Qu, Y., Zhang, B., & Kumar, P. 2023, MNRAS, 518, 66
Rajwade, K., Wharton, R., Majid, W., et al. 2022, ATel, 15791, 1
Rajwade, K. M., Mickaliger, M. B., Stappers, B. W., et al. 2020, MNRAS, 495, 3551
Ransom, S. M. 2001, PhD thesis, Univ. Harvard
Ravi, V. 2022, ATel, 15693, 1
Ravi, V., Catha, M., Chen, G., et al. 2023, ApJL, 949, L3
Scargle, J. D. 1982, ApJ, 263, 835
Seymour, A., Michilli, D., & Pleunis, Z. 2019, DM_phase: Algorithm for Correcting Dispersion of Radio Signals, Astrophysics Source Code Library, ascl:1910.004
Sheikh, S., Farah, W., Pollak, A. W., et al. 2022, ATel, 15735, 1
Wang, F. Y., Zhang, G. Q., Dai, Z. G., & Cheng, K. S. 2022a, NatCo, 13, 4382
Wang, W.-Y., Jiang, J.-C., Lee, K., Xu, R., & Zhang, B. 2022b, MNRAS, 517, 5080
Wang, W.-Y., Yang, Y.-P., Niu, C.-H., Xu, R., & Zhang, B. 2022c, ApJ, 927, 105
Xu, H., Niu, J. R., Chen, P., et al. 2022, Natur, 609, 685
Yang, Y.-P., Xu, S., & Zhang, B. 2023, MNRAS, 520, 2039
Yang, Y.-P., & Zhang, B. 2018, ApJ, 868, 31
Yao, J. M., Manchester, R. N., & Wang, N. 2017, ApJ, 835, 29
Yu, Z., Deng, F., Niu, C., et al. 2022, ATel, 15758, 1
Zhang, B. 2022a, arXiv:2212.03972
Zhang, B. 2022b, ApJ, 925, 53
Zhang, R. C., Zhang, B., Li, Y., & Lorimer, D. R. 2021, MNRAS, 501, 157
Zhang, Y., Niu, J., Feng, Y., et al. 2022a, ATel, 15733, 1
Zhang, Y. G., Gajjar, V., Foster, G., et al. 2018, ApJ, 866, 149
Zhang, Y.-K., Wang, P., Feng, Y., et al. 2022b, RAA, 22, 124002
Zhao, Z. Y., Zhang, G. Q., Wang, F. Y., & Dai, Z. G. 2023, ApJ, 942, 102
Zhou, D. J., Han, J. L., Zhang, B., et al. 2022, RAA, 22, 124001